Dimensions of the deposited strand in the material extrusion process: Experimental and numerical investigations

D. Xu, J.-F. Agassant, F. Pigeonneau*

MINES Paris, PSL Research University, CEMEF - Centre for materials forming, CNRS UMR 7635, CS 10207, rue Claude Daunesse 06904 Sophia Antipolis Cedex, France

Abstract

The material extrusion process is investigated by focusing on the geometry of a single strand extruded through a printing nozzle and deposited on a substrate of a 3D printer. An experimental protocol is set to determine the width W, and the height H, of a strand. The geometry depends mainly on the nozzle diameter D, the gap between the substrate and the tip of the nozzle g, the extrusion velocity U and the printing velocity V. The relevant parameter to determine W/D and H/g is reduced to one dimensionless parameter equal to $(D/g)(U/V)$.

A computational multiphase flow is described using a level set approach and a finite element method. The heat transfer is also taken into account in the set of governing equations. The polymer is considered as a generalised Newtonian fluid. An accurate description of the interface between the polymer and the surrounding air is developed based on an anisotropic remeshing procedure.

Two different situations are numerically solved for which: (i) a first case with a g/D ratio less than one and (ii) a second case with a g/D ratio larger than one. In the first situation, the spreading below the nozzle is more or less radial around the vertical axis of the extruder which is not the case in the second situation. The numerical shape geometry is in good agreement with experimental observations. The thermal cooling underlines that the relevant parameters are the perimeter and the area of the strand cross-section and the Péclet number based on the printing velocity. The numerical predictions of W/D and H/g agree with experimental results.

Keywords: material extrusion; polymer; cross-sectional geometry; heat transfer; finite element analysis

*Corresponding author: Tel. +33 (4) 93 95 74 34.
Email address: franck.pigeonneau@minesparis.psl.eu (F. Pigeonneau)

1. Introduction

The material extrusion process, also known under the name of Fused Filament Fabrication (FFF), is an additive manufacturing technology mainly used with thermoplastic polymers. The FFF process deposits melted filaments of polymer layer upon layer to build an object designed with a Computer-Aided Design (CAD) software. A solid filament of polymer is fed into a liquefier with a pinch roller mechanism. The polymer is heated above its melting temperature in the liquefier and then deposited on a surface. The desired object is obtained after solidification of the polymer. According to Bellini et al. [1], the geometry of the liquefier can be divided in three areas: (i) the neat filament is introduced and melted in an upstream cylindrical part; (ii) it is then forced through a convergent; (iii) it is extruded through a capillary. This simple view of the process underlines the transient character of the process. While the residence time of the polymer is roughly around two seconds in the liquefier, the material undergoes heating, large deformation and cooling. By nature, the deposition of a filament is an out of equilibrium process. The determination of the strand dimensions is not a simple task. These predictions are useful to better calibrate the deposition path as a function of the geometry of the printed object. The purpose of the current article is to address the shape of a filament under a point of view of fluid mechanics and thermal heat transfer.

Geometry, kinematic and thermal parameters govern the FFF process such as (i) the gap distance between the nozzle and the depositing surface g, (ii) the diameter of the nozzle D, (iii) the extrusion velocity U, (iv) the printing velocity V, (v) temperatures of the liquefier, substrate, and surrounding air. Material properties have a dominant influence on the extrusion and the deposition steps. Using a finite element analysis, Bellini [2] investigated the influence of the printing head on the strand shape. The viscosity of the polymer is described using a power law coupled with an Arrhenius law to take into account the temperature dependence. When the gap is small, the flattening of the top surface was underlined. The velocity and the temperature fields are also described during the strand deposition. These simulations are in good agreements with experimental observations in terms of geometry and temperature distribution.

Arguing a simple dimensional analysis, the major parameters influencing the strand shape are g/D and U/V ratios. Hebda et al. [3] studied the influence of the gap distance, extrusion, and printing velocities on the strand geometry. To determine width and height, the strand cross sections were measured by micro CT-imaging. An empirical relation between the strand width and the square root of the velocity ratio U/V is proposed for ABS and PLA polymers. According to Hebda et al. [3], the deposited strand width does not depend on the g/D ratio. Furthermore, they argued that the cross section is close to an elliptic shape.

Comminal et al. [4] computed the strand shape by modelling the flow field with a finite volume method. The interface between the polymer and the air is tracked by a coupled level-set/volume-of-fluid method. The polymer is considered as an incompressible, isothermal, and Newtonian fluid. Two dimensionless parameters are investigated: the velocity ratio V/U and the normalised gap g/D. The strand thickness is not always equal to the gap and varies between -10 to $+35\,\%$ of the gap. By performing optical microscopy measurements, Serdeczny et al. [5] assessed the strand geometry found by Comminal et al. [4]. Based on a volume-of-fluid method, Gosset et al. [6] performed numerical simulations of strand deposition. The temperature is assumed uniform. The polymer viscosity is described by a Cross power law. They measured the strand lateral geometry by recording the deposition with a high-speed video camera. They found good agreements with numerical results. The experimental protocol allowed to highlight the influence of the nozzle velocity on irregularities of the strand surface. Behdani et al. [7] used different constitutive equations, with and without thermal coupling. They showed that a temperature dependent power law behaviour provides the best ageement with Serdeczny et al.'s experiments [5]. Agassant et al. [8] proposed an analytic model for the strand deposition shape based on a Stefan flow around the nozzle and a no-slip boundary condition all along the bottom of the nozzle. Simple relations for the strand height and width are proposed. These approximate solutions are compared to numerical computations achieved for an incompressible Newtonian fluid in isothermal condition. Xia et al. [9, 10, 11, 12] computed the strand deposition based on a front tracking/finite volume method. They highlighted the importance of the visco-elastic behaviour of the polymer. When the viscoelasticity is taken into account, an increase of the deposited strand height and a decrease of the strand width are found.

As the above referred authors, experimental measurements of the single strand deposition have been performed on a wide series of printing conditions. The originality of our paper is to express the strand height and width as a function of a unique dimensionless parameter issued from our previous analytical model [8]. To complete experimental investigations, a finite element analysis coupling fluid dynamics and heat transfer is achieved. An accurate remeshing procedure allows to precisely capture the interface between the polymer and surrounding air.

The paper is organised as follows: The experimental measurements of strand shape are presented in section 2. Optical microscopy measurements are done on strands printed with two different nozzle diameters D, with different gaps g, various extrusion velocities U and nozzle velocities V. The numerical analysis of the strand shape is developed in section 3 for two cases. Section 4 is devoted to the comparison of experimental and numerical predictions. The last section summarises the main results and presents few

perspectives. A nomenclature is provided in Appendix A. The numerical procedure developed to study the fluid dynamics of the polymer deposition is detailed in Appendix B.

2. Experimental analysis of strand cross-sectional geometry

2.1. Materials

Experiments and numerical computations are achieved with an acrylonitrile butadiene styrene (ABS), polymer commonly used in the FFF process. The ABS is purchased as neat filaments from Grossiste3D®. According to the supplier, the density is equal to $1010\,\mathrm{kg/m^3}$ at room temperature. The glass transition temperature is measured by Differential Scanning Calorimetry (DSC) on a DSC4000 from PerkinElmer®. The value of T_g is found equal to $105\,^{\circ}\mathrm{C}$. The specific heat capacity at constant pressure and thermal conductivity are taken from [13]. Table 1 summarises these properties.

Table 1: Properties of the ABS polymer used in numerical computations. The values of C_p and k are taken from [13].

ρ	C_p	k	T_g
$\mathrm{kg/m^3}$	$\mathrm{Jkg^{-1}K^{-1}}$	$\mathrm{W\,m^{-1}\,K^{-1}}$	°C
1010	2100	0.21	105

Rheology measurements are performed on a parallel plate rheometer ARES from TA Instruments® in dynamic oscillations. Measurements are done at 1 % strain on a frequency range from 0.1 to $100\,\mathrm{rad\,s^{-1}}$ and a temperature range from 210 to 240 °C. The different viscosity curves are then shifted to a reference temperature of 220 °C by introducing a shift factor a_T, see [14] for more details. The obtained general curve is then fitted by a Carreau-Yasuda law given by

$$\eta(T,\dot{\gamma}) = \frac{\eta_0 a_T}{\left[1+(a_T\lambda\dot{\gamma})^a\right]^{\frac{1-m}{a}}}, \tag{1}$$

with η_0 the Newtonian (or zero shear rate) viscosity, λ the relaxation time, $\dot{\gamma}$ the shear rate, a the Yasuda coefficient controlling the transition between the Newtonian plateau and the power law regime and m the shear thinning or power law index. The temperature dependence of the rheological data is integrated via a shift factor a_T following an Arrhenius law:

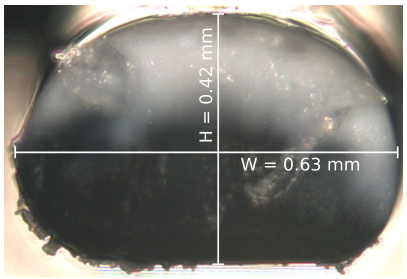
$$a_T = \exp\left[\frac{E_a}{R}\left(\frac{1}{T}-\frac{1}{T_{\mathrm{ref}}}\right)\right], \tag{2}$$

with R the ideal gas constant, E_a the polymer activation energy and T_{ref} the reference temperature. Table 2 gathers the fitted parameters of equations (1) and (2).

Table 2: Fitting parameters of the Carreau-Yasuda and Arrhenius laws for the ABS.

η_0	λ	a	m	E_a	T_{ref}
$\text{Pa} \cdot \text{s}$	s	-	-	kJ mol^{-1}	°C
3.04×10^3	3.2×10^{-2}	0.6	0.27	115.05	220

(a) U=4 m min^{-1}, V=2 m min^{-1}.



(b) U=5 m min^{-1}, V=1 m min^{-1}.

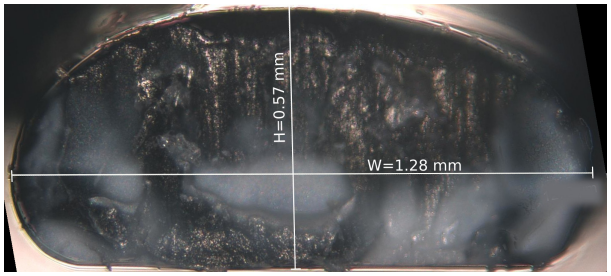


Figure 1: Strand cross section measured with an optical microscope. The printing is performed at g=0.6 mm and D=0.4 mm.

2.2. Cross-sectional geometry of a single strand

An experimental protocol is developed to measure the strand shape as a function of the printing conditions. Single strand deposition is done using an Original Prusa i3 MK3 from the brand Prusa®. The strands are printed as a function of the U/V ratio for different printing velocities V. All samples have a length of 10 cm. The printing velocity is an explicit parameter in the G-code file written to print the strand. The extrusion velocity is indirectly assigned by setting the length of neat filament extruded through the liquefier. The desired U is computed by mass balance as stated by Xu et al. [15]. The temperature of the extruder is set equal to 230 °C and the temperature of the substrate is set equal to 94 °C.

The strand is cut at approximately one half of its length. Its shape is observed using an optical microscope Olympus® PMG3 in reflection mode. For a given ratio U/V, around ten printed strands are measured. The average width and height are computed for a given set of printing velocities. Examples of strand measurements are shown in Figure 1 for which the gap is set to 0.65 mm with a nozzle diameter of 0.4 mm. The filament width increases significantly when the extrusion velocity increases. While the gap is the same between the two experiments shown in Figure 1, the width is three time larger when U/V is equal to 5 than when U/V is equal to 2. The height does not change in large proportion.

These two examples underline the asymmetric shape of the cross section of the strand. The contact with the substrate leads to a flattening of the polymer. The upper part of the strand is more similar to an elliptic shape. These cross section geometries correspond

to a case for which g is larger than D.

In the following, the analysis is focused on the two main characteristics of the cross section, i.e. the width W and the height H.

2.3. Strand width as a function of the printing parameters

The determination of the strand shape deposited by the FFF process is a problem of fluid dynamics. A simple dimensional analysis leads to consider the behaviour of W/D as a function of g/D, and U/V ratios. Of course, other dimensionless numbers should be involved, like Reynolds or capillary numbers among others. As it will be justified latter, the Reynolds number is small enough to be considered as irrelevant. The capillary number is much larger than one meaning that viscous effects are dominant compared to surface tension as it has been shown by Gosset et al. [6]. Experiments are done with two nozzles with D equal to 0.4 and 0.3 mm. The g/D ratio varies in the range of $[0.5; 1.625]$. The velocity ratio is in the range of $[1.5; 5]$. To confirm the weak influence of the printing velocity, experiments have been achieved for two values of V.

According to Hebda et al. [3], experimental values of W/D are represented as a function of $\sqrt{U/V}$. Figure 2 gathers W/D as a function of $\sqrt{U/V}$ obtained experimentally. Data have been plotted for four g/D ratios. For a given g/D ratio, W/D scales linearly with $\sqrt{U/V}$.

The decrease of g/D ratio leads to an increase of W/D. When the g/D ratio is larger than one, there is no squeezing effect between the substrate and the nozzle especially for low viscoelastic polymers. This is supposed to be the case for the ABS polymer due to the low value of λ given in Table 2. When g is lower than D, the polymer is squeezed between the nozzle and the substrate. This effect is even more important for a large value of U/V. This trend can be explained by the pressure applied on the polymer. Figure 2 pinpoints that this squeezing effect is least for g/D equal to 0.5. At large values of $\sqrt{U/V}$, the strand width obtained for g/D equal to 0.5 is close to the results obtained at g/D equal to 0.8.

The scaling in $\sqrt{U/V}$ has not be explained in [3] as well as the dependence of the g/D ratio pointed out in Figure 2. In our previous contribution [8], the shape of the strand has been analysed using a simplified analytical model of the flow around the nozzle. The length L over which the polymer is spread in the front of the nozzle is given by

$$L = \frac{-R_n + \sqrt{(R_n - D)^2 + \frac{\pi D^2}{g}\frac{U}{V}\left(R_n - \frac{D}{2}\right)}}{2}, \tag{3}$$

with R_n the external radius of the nozzle. The spreading on the side is assumed to be the same as the spreading in the front of the nozzle. The strand section is considered as

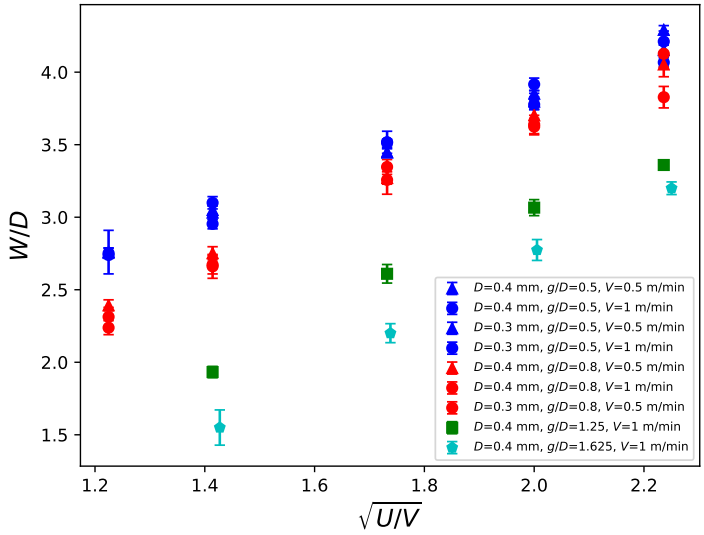


Figure 2: W/D as a function of $\sqrt{U/V}$ obtained experimentally for two printing velocities, two nozzle diameters and four g/D ratios.

a rectangular shape. The strand width is then given by the following relation

$$\frac{W}{D} = 1 - \frac{R_n}{D} + \sqrt{\left(\frac{R_n}{D} - 1\right)^2 + \frac{\pi D}{g}\frac{U}{V}\left(\frac{R_n}{D} - \frac{1}{2}\right)}. \tag{4}$$

According to the geometry characteristics of the nozzle [16], the first term, $(R_n/D - 1)^2$, in the square root is much less than the second term. It can thus be neglected as a first approximation. The strand width is expected to depend predominantly on

$$\alpha = \frac{D}{g}\frac{U}{V}. \tag{5}$$

The ratio W/D is plotted as a function of $\sqrt{\alpha}$ for the data of Figure 3. The data clearly fall in a single curve when the g/D ratio is larger or equal to 0.8.

At small $\sqrt{\alpha}$ values, W/D seems to be a linear function. When $\sqrt{\alpha}$ increases the slope decreases and the curve takes the shape of a parabola which justifies introducing an additional term function of α. The solid line in Figure 3 is a fitted solution written as follows

$$\frac{W}{D} = -2.073 + 4.059\sqrt{\alpha} - 0.659\alpha. \tag{6}$$

Results for the g/D ratio equal to 0.5 are singular and the fitting curve has been done without these data. This will require more investigations. Notice also that this analysis

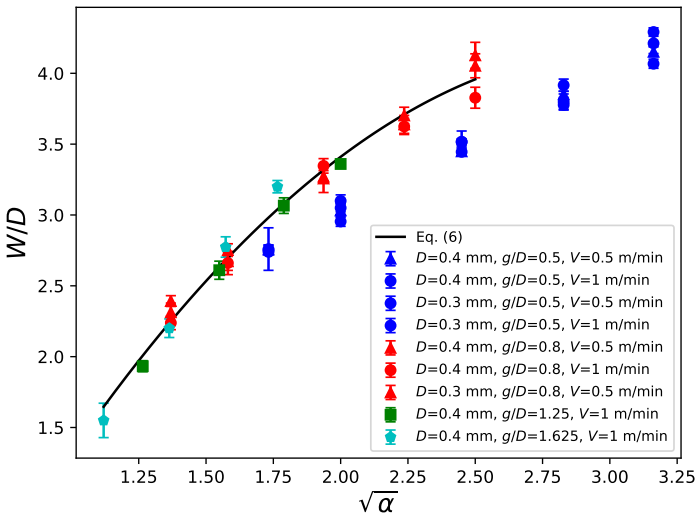


Figure 3: W/D as a function of $\sqrt{\alpha}$ obtained experimentally for two printing velocities, two nozzle diameters and four g/D ratios.

has been done for a particular polymer and without changing the thermal conditions.

2.4. Strand height as a function of the printing parameters

The area of the deposited strand is related to the U/V ratio by a simple mass balance as follows [3, 15]

$$A = \frac{\pi D^2}{4}\frac{U}{V}. \tag{7}$$

The knowledge of the strand width leads to the determination of its height through the mass balance and assuming an elliptic strand shape [3]:

$$\frac{H}{D} = \frac{U}{V}\frac{D}{W}. \tag{8}$$

Figure 4 depicts the H/D ratio as a function of U/V for different g/D ratios obtained experimentally. A linear trend of H/D as a function of U/V appears. The height of the strand increases with g/D ratio with the same explanation as for the strand width. When g/D is lower than one, the strand is squished between the substrate and the nozzle. When g/D is larger than one, the strand height is free to develop. The dispersion for the various g/D values is important which limits the possibility to find a general synthesis of these data.

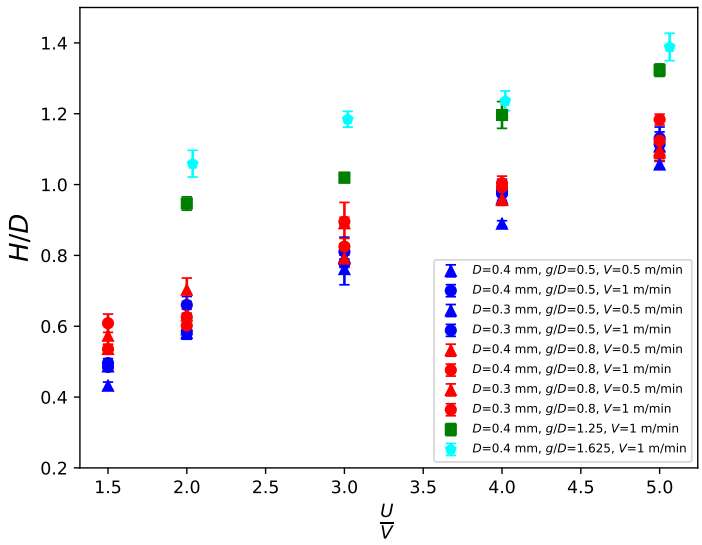


Figure 4: H/D as a function of U/V obtained experimentally for two printing velocities, two nozzle diameters and four g/D ratios.

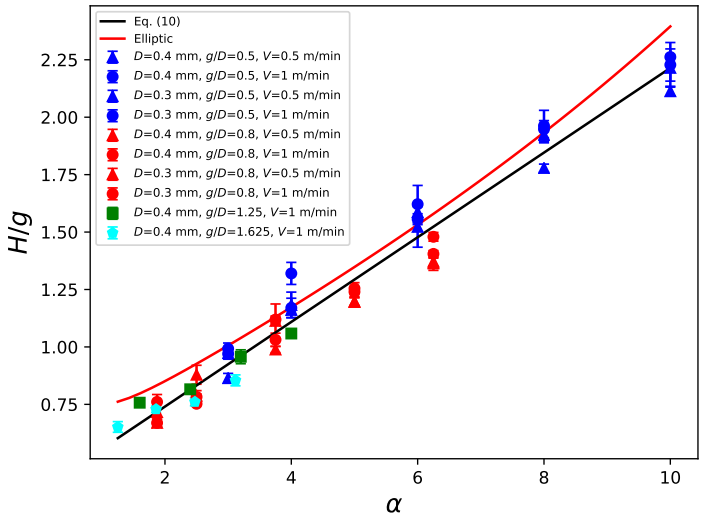


Figure 5: H/g as a function of α obtained experimentally for two printing velocities, two nozzle diameters and four g/D ratios.

Equation (8) allows to write H/g as follows

$$\frac{H}{g} = \frac{D}{g}\frac{U}{V}\frac{D}{W} = \frac{\alpha D}{W}. \tag{9}$$

Since W/D is a function of α, it is expected to find a scaling of H/g as a function of the same parameter. Figure 5 provides the behaviour of H/g as a function of α. A linear single curve is observed. It is noteworthy that the data obtained for g/D equal to 0.5 are in agreement with the other g/D ratios. The black solid line represents the solution obtained by a linear regression given by

$$\frac{H}{g} = 0.372 + 0.184\alpha. \tag{10}$$

The red solid line is a solution using equation (9) and the fitting equation (6). Figure 5 shows that this solution is equivalent to the preceding one with a slight shift on the ordinate values.

The knowledge of the strand width and height is of prime importance for the setting of the deposition path to build an object with the desired infill. The empirical model gives a good first approximation of the strand height. The discrepancies between experimental data and equation (10) do not exceed 16 %.

3. Numerical prediction of the strand shape

In parallel of the experimental work, numerical computations have been achieved with our own finite element `C++` library. The numerical investigations focus on the polymer spreading around the extruder. Both the polymer and the surrounding air are accounted for. The fluid dynamics of this multiphase problem is considered as a single-fluid representation using a level set method [17, 18]. The polymer is considered as a temperature dependant generalised Newtonian fluid. The dynamic viscosity is given by the Carreau-Yasuda law, eq. (1). Both polymer and air are considered as incompressible. Since the process is achieved in an open system, the overall pressure does not change significantly to modify the air density. Moreover, the thermal gradients are not strong enough to consider thermal dilatation of the surrounding air. The interface between the two phases leads to consider the surface tension. This supplementary force is added using the continuum surface force proposed by Brackbill et al. [19]. The heat transfer equation is also considered. The viscous dissipation is neglected.

The reference frame is attached to the nozzle. This means that the motion is simply considered by sliding the substrate in the opposite direction of the motion of the extruder. In this work, only a uniform motion is considered.

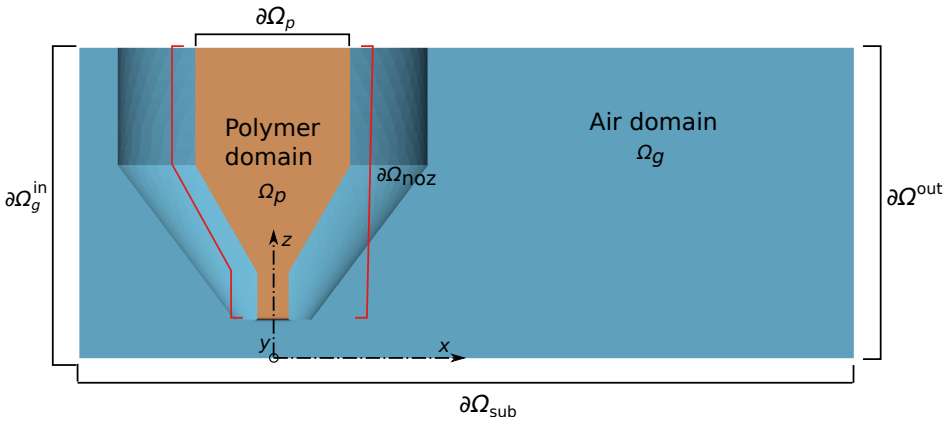


Figure 6: Partial view in the symmetric plane of the domain in the initial state with the two subdomains and the main boundaries.

Figure 6 shows the cut in the symmetric plane of the computational domain. The geometry of the nozzle is taken from the design of the E3D-V6 nozzle [16]. Initial positions of the polymer and air domains are depicted. The main boundaries are also indicated.

Following the best practices in fluid mechanics, the governing equations are normalised to reduce the number of parameters. Since the work is focused at a scale corresponding to the gap between the tip of the nozzle and the substrate, the spatial dimensions are scaled by g. The characteristic velocity is the printing velocity, V. All physical properties, density, dynamic viscosity, heat capacity, thermal conductivity are normalised by the properties of the polymer given in Table 1. The characteristic viscosity is taken on the Newtonian plateau given in Table 2.

The thermal problem is driven by the extruder temperature, T_{ext}, the substrate temperature, T_{sub} and the temperature of the surrounding air, T_{air}. The reduced temperature is given by

$$\theta = \frac{T - T_{\text{air}}}{T_{\text{ext}} - T_{\text{air}}}, \tag{11}$$

to have a dimensionless temperature ranging from 0 and 1.

Apart from the aspect ratio, g/D and the velocity ratio U/V, four dimensionless numbers are needed to solve the numerical problem. The Reynolds number, Re, the capillary number, Ca, the Péclet number, Pe and the Weissenberg number, Wi, are

Table 3: Values of dimensionless numbers for the two numerical simulations.

g/D	0.75	1.625
Re	2.77×10^{-6}	3.60×10^{-6}
Ca	1748.5	1748.5
Pe	84.17	109.42
Wi	1.78	0.82

defined by

$$\mathrm{Re} = \frac{\rho_p V g}{\eta_0}, \tag{12}$$

$$\mathrm{Ca} = \frac{\eta_0 V}{\gamma}, \tag{13}$$

$$\mathrm{Pe} = \frac{\rho_p C_{p_p} V g}{k_p}, \tag{14}$$

$$\mathrm{Wi} = \frac{\lambda V}{g}. \tag{15}$$

As a purely viscous behaviour is considered, the Weissenberg number Wi is only used to make the parameter λ of eq. (1) dimensionless. In Ca, γ is the surface tension between the polymer and the air. According to Bellehumeur et al. [20], γ is taken equal to $2.8 \times 10^{-2}\,\mathrm{N\,m^{-1}}$. The substrate, the nozzle and the air temperatures are taken equal to 94, 230 and 40 °C, respectively. In the initial state, the polymer temperature inside the nozzle is taken equal to the nozzle temperature.

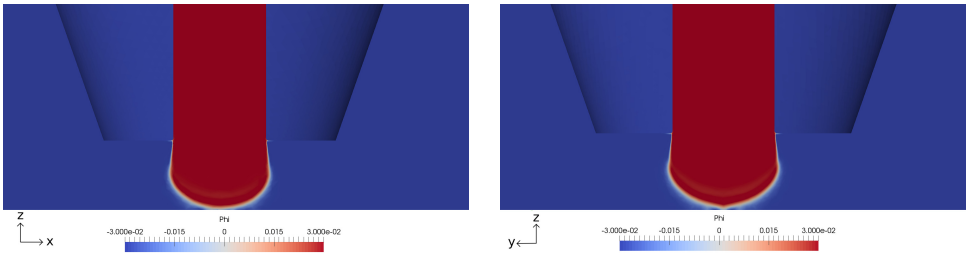
To be self-contained, the governing equations, the boundary conditions and the numerical method are detailed in Appendix B.

3.1. Spreading dynamics for a g/D ratio smaller and larger than one

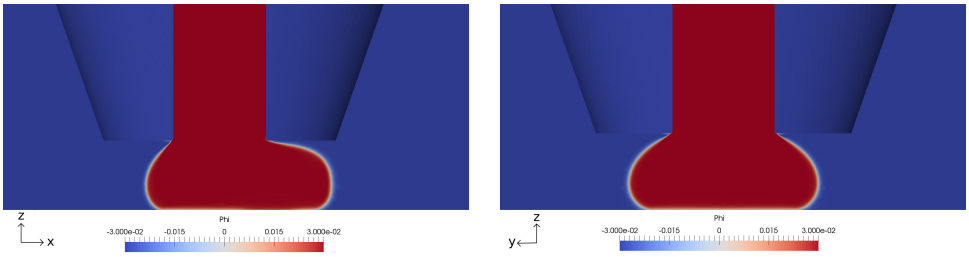
From the experimental analysis, the spreading behaves differently if g/D ratio is either smaller or larger than one. The main characteristics of the spreading are carefully analysed when g/D is equal to 0.75 and 1.625. Numerical runs are achieved for the nozzle diameter equal to 0.4 mm and a printing velocity V equal to $1\,\mathrm{m\,min^{-1}}$. The Reynolds, capillary, Péclet and Weissenberg numbers are summarised in Table 3. The dimensionless numbers show that inertia and surface tension have a weak effect.

Figure 7 shows the polymer spreading at three successive time steps with g/D equal to 3/4 and U/V equal to 3. Blue and red colours correspond to the surrounding air and the polymer phases, respectively. The interface position corresponds to the zero-value of the level set function. The first column of Figure 7 represents the view in the symmetric plane, $(x, 0, z)$ while the second column is the view in the $(0, y, z)$ plane perpendicular to the symmetric plane. The well captured interface results from the

(a) t=5.13 $\times$ 10^{-3} s



(b) t=1.863 $\times$ 10^{-2} s



(c) t=5.643 $\times$ 10^{-2} s

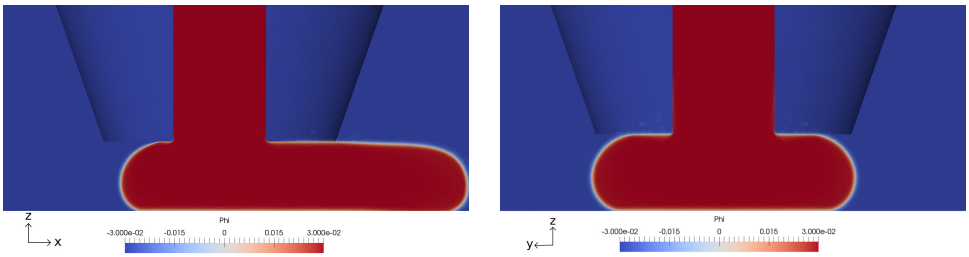


Figure 7: Snapshots of the polymer spreading at the exit of the nozzle at the first steps of the deposition for g/D=3/4 and U/V=3. The first column corresponds to the view in the symmetric plane and the second column, to the view in the transversal $(0, y, z)$ plane.

refined mesh adaptation around the interface performed at each time step. The numerical computation thus allows to study the behaviour of the interface with high accuracy.

The first considered time step corresponds to the contact of the polymer with the substrate. The polymer exhibits a quasi-axisymmetric shape. A slight die swell is observed even if the viscoelastic behaviour is not accounted for. This corresponds to the die swell of a purely viscous fluid without gravity and inertia effects [21]. For t=1.863 $\times$ 10^{-2} s, the polymer is drawn by the substrate. Due to a large value of U/V, a slight spreading of the polymer is observed upstream to the deposition. The polymer spreads transversely. When t=5.643 $\times$ 10^{-2} s, the polymer is in contact with the nozzle and substrate. At the same time, the polymer spreading upstream is stabilised. The squeezing of the poly-

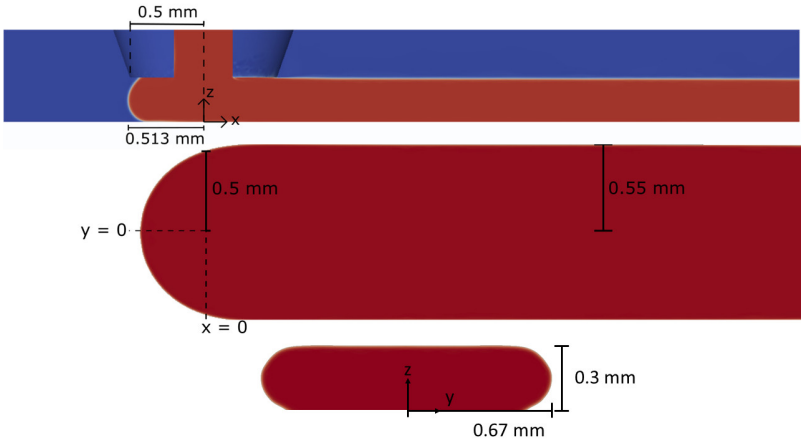


Figure 8: Geometry of the polymer strand for g/D=0.75, U/V=3 for a nozzle diameter equal to 0.4 mm and V=1 m min^{-1} in the steady-state regime.

mer is important for this set of working conditions. However, the polymer spreading upstream does not flow beyond the edge of printing head. In that case, it could disrupt the displacement of the printer head.

For this first set of working conditions, Figure 8 shows the shape of the strand in the three planes (x, y), (x, z) and (y, z) when the steady-state regime is reached. This state is established when the morphology of the filament does not change with time. The steady-state regime is reached for t equal to 0.388 s. This time corresponds to a deposition length of around 6.5 mm. The polymer remains in contact with the tip of the printing head. It spreads radially from the extruder axis over a radius equal approximately to 0.5 mm. These pictures agree with the approach developed in [8]. The analytical solution of the length L given in Equation (3) is compared to the simulation result. The analytical solution gives L equal to 0.37 mm while L is equal to 0.39 mm in the numerical computation. The prediction shows 6 % deviation for g/D=0.75. Far from the extruder, the strand spreads wider than the exterior size of the tip of the nozzle. The shape of the strand is very similar to an oblong shape with a height approximately equal to the gap g.

The successive deposition steps when g/D is equal to 1.625 are shown in Figure 9. As in the previous case, the first time step is chosen when the polymer is just touching the substrate. A slight die swell is also observed. At t=4.036 $\times$ 10^{-2} s, Figure 9(b) shows that the polymer is already drawn by the substrate. The contact area is very small as it is clearly seen in the perpendicular view to the symmetric plane. For t=8.716 $\times$ 10^{-2} s, the contact area stays also moderate. As expected, when g/D is larger than one, the polymer is not confined between the substrate and the nozzle. The polymer does not

touch the tip of the nozzle.

Figure 10 depicts the steady-state regime of the strand. This regime is reached after 0.647 s. This corresponds to a deposition of 1 cm. The transverse spreading is weak because the extruded polymer is not restrained by the nozzle anymore. The same trend is observable upstream, at the front of the nozzle.

In the steady-state regime, the strand shape is close to a half disk around the nozzle and then reaches a uniform shape downstream. The morphology of this half disk depends on g/D. The transition between the two shapes occurs on a longer distance when the g/D ratio increases. Anyway, in each printing situation, a stabilised deposit shape is achieved within few millimetres.

As already shown in the experimental analysis, the gap distance has an impact on the dimensions and geometry of the deposited strand. For a given printing ratio U/V, the shape is more oblong when the gap is smaller than the nozzle diameter. In the opposite case, the shape is more ellipsoidal. When g/D is equal to 0.75, the polymer is in contact with the nozzle wall. The resulting strand shape has a more planar upper surface. As seen in Figure 8, the strand maximum height is very close to the gap, i.e. 0.3 mm, and the width is 1.33 mm. On the other hand, for g/D larger than one, the gap does not impact so much the strand shape. As shown in Figure 10, H is equal to 0.49 mm and W=0.9 mm.

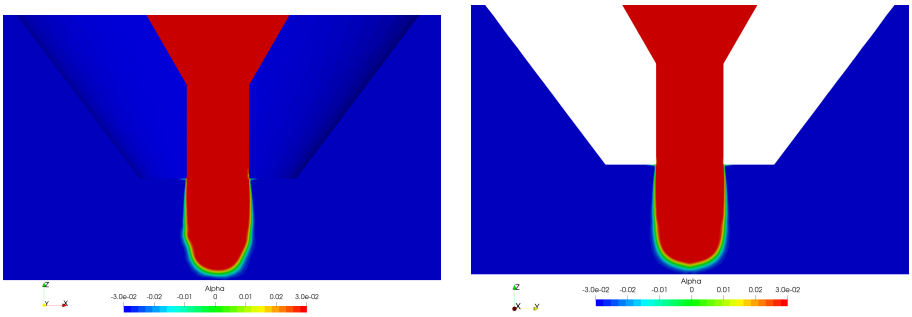
3.2. Velocity and pressure fields

Figures 11 and 12 represent the x component of the velocity field in the symmetric plane for g/D equal to 0.75 and 1.625 respectively. Once again, the two situations are very different. When the gap is lower than the nozzle diameter, Figure 11, the maximum of the velocity is observed close to the tip of the nozzle. Apart from the nozzle exit, the velocity is completely uniform with a velocity magnitude equal to the printing velocity.

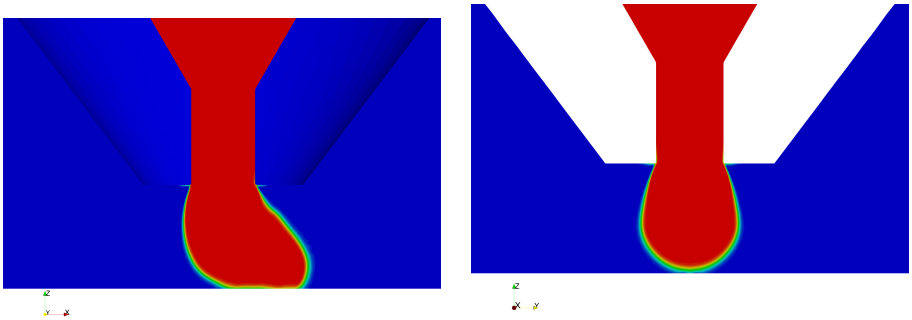
When g/D is equal to 1.625, Figure 12, the x component of the velocity field behaves differently. Apart from the free surface on the left side of the nozzle, the velocity becomes quite immediately uniform close to the nozzle exit and equal to the printing velocity. For both cases depicted here, the polymer undergoes a shear flow only close to the nozzle exit. When the polymer is out this area, it is just drawn by the wall with a uniform velocity. With low shear rate and a temperature decreasing, the viscosity of the polymer increases strongly leading to a vanishing rate of strain tensor. In other words, the polymer behaves like a solid.

Figure 13 depicts the vertical profile of the x component of the velocity field for both cases at a particular downstream location x=0.35 mm just before the periphery of the nozzle (see in Figures 11 and 12). The black solid and dashed lines are the numerical solution for g/D ratio equal to 0.75 and 1.625, respectively. In the situation of a small

(a) t=1.696 $\times$ 10^{-2} s



(b) t=4.036 $\times$ 10^{-2} s



(c) t=8.716 $\times$ 10^{-2} s

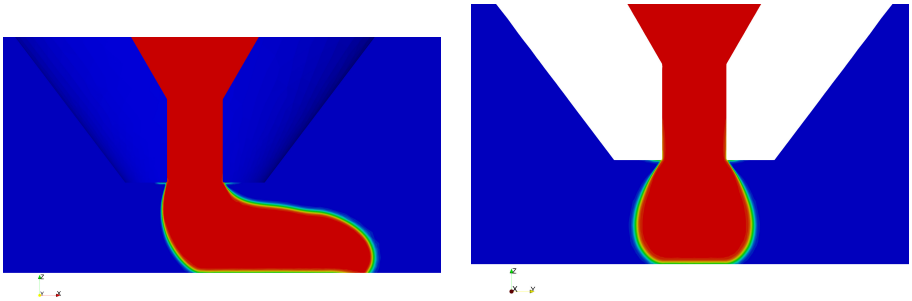


Figure 9: Snapshots of the polymer spreading at the exit of the nozzle at the first steps of the deposition for g/D=1.625 and U/V=3. The first column corresponds to the view in the symmetric plane and the second column, the transversal view cutting the extruder in two equal parts.

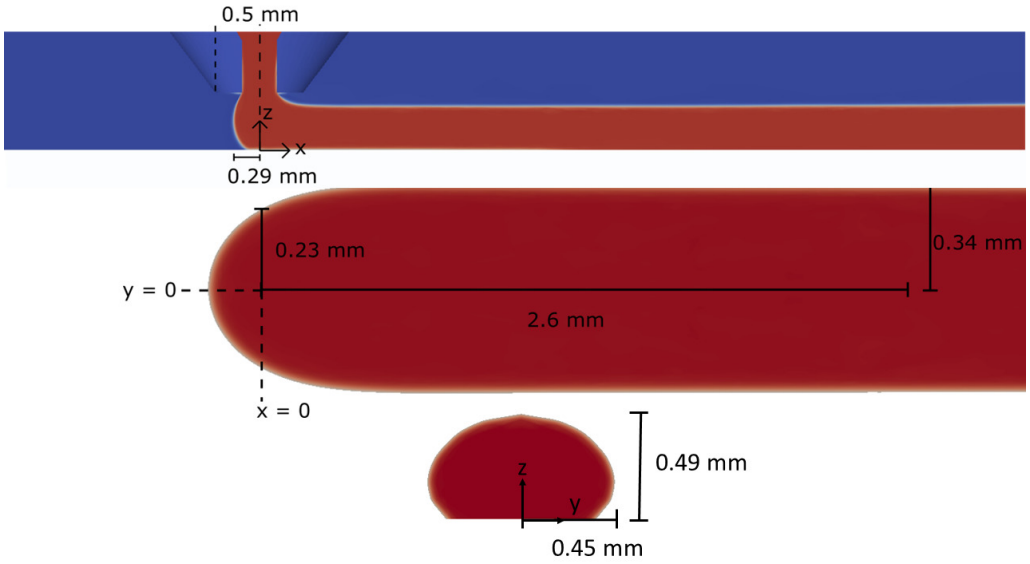


Figure 10: Geometry of the polymer strand for g/D=1.625, U/V=3 for a nozzle diameter equal to 0.4 mm and V=1 m min^{-1}.

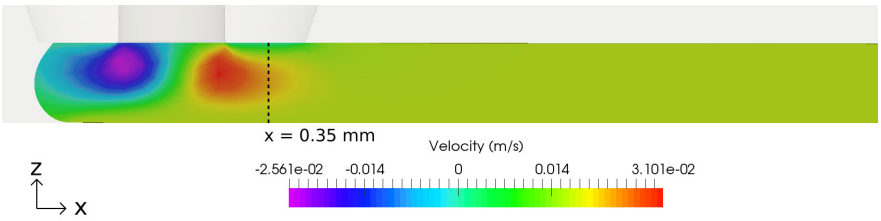


Figure 11: Velocity field in the (x, z) plane for g/D=0.75.

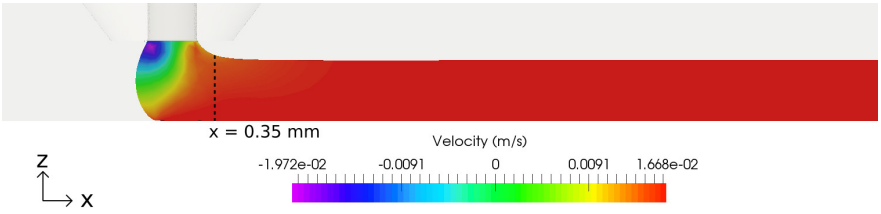


Figure 12: Velocity field in the (x, z) plane for g/D=1.625.

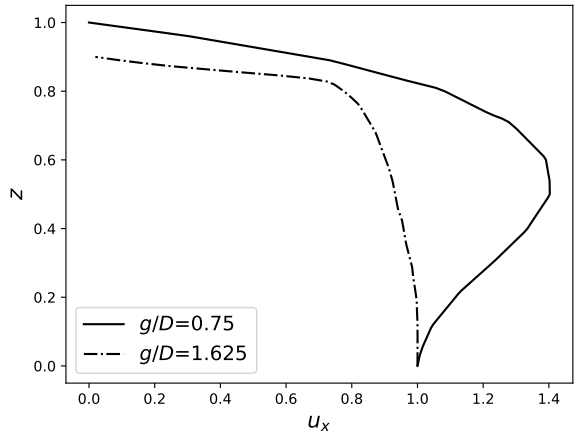


Figure 13: Velocity profile u_x at x=0.35 mm for both gaps.

gap, i.e. g/D=0.75, the polymer is in contact with the substrate and the nozzle. For a purely viscous fluid, the velocity is the sum of a shear flow induced by the displacement of the nozzle and the injection of the polymer between the two parallel horizontal planes. Notice that at this particular location, the shear rate is equal to zero on the substrate.

In the case of large gap, the extrusion velocity is too low to spread the polymer radially. The presence of the free surface leads to a vanishing shear stress. The x component of the velocity is a quasi-plug flow profile. It decreases at the upper free surface due to reorientation of the strand. This situation is close to the imposed kinematics of McIlroy and Olmsted [22]. When g/D is less than one, the velocity profile is more complex than the one used in the work of McIlroy and Olmsted [22].

The pressure field is depicted in the (x, y) plane in Figure 14 for both gaps investigated in this section. When the ratio g/D is equal to 0.75, the pressure field is radially distributed around the axis of the extruder. This means that the flow due to the extrusion prevails. For g/D equal to 1.625, the pressure field is strongly different. The amplitude is 8.8 times smaller than the case with a g/D ratio equal to 0.75. The motion of the substrate drives the pressure field giving an asymmetric pressure distribution.

When the g/D ratio decreases, the pressure on the substrate increases due to the contact of the nozzle with the polymer. Increasing the pressure will favour welding [23] and decrease porosity. When g/D=1.625, the contact of the nozzle with the polymer is strongly reduced in the detriment of welding and porosity removal.

3.3. Thermal cooling

The adhesion quality is influenced by the thermal cooling. Heat transfer during the filament deposition depends on the cooling with the surrounding air and the contact

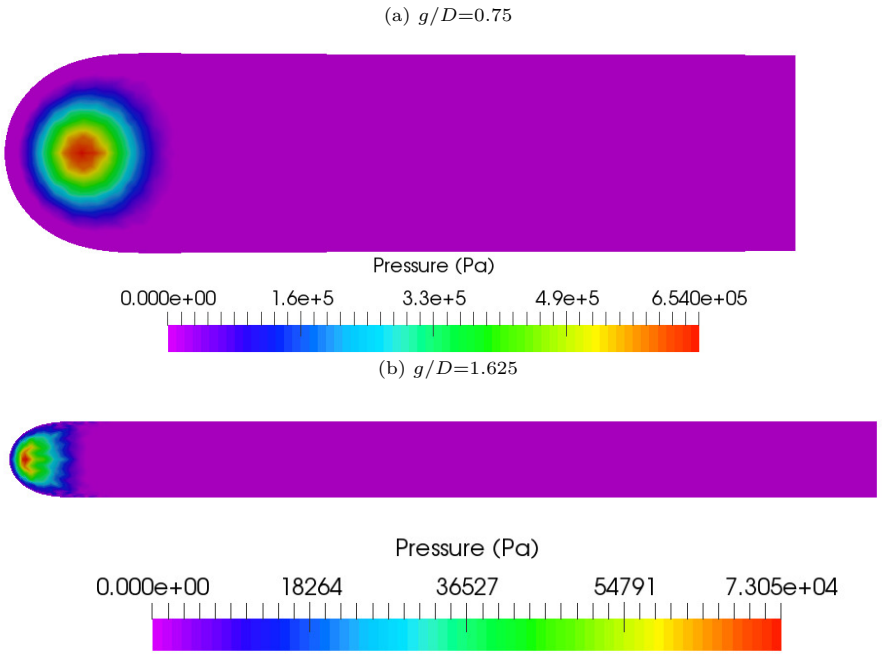


Figure 14: Pressure field in the (x, y) plane for (a) g/D=0.75 and (b) g/D=1.625.

with the substrate. In the single strand printing situation considered here, the interface temperature between the metallic substrate and the deposited strand will be near the temperature of the substrate due to the large effusivity of the metallic substrate. In the case of the deposition of successive stands, the interface temperature will be the arithmetic average between the previously and the newly deposited strands. In Figure 15, the temperature field is shown for g/D equal to 0.75 in the symmetric plane and in the cross section localised at x=3.23 mm from the nozzle exit. While the temperature is supposed uniform at the tip of the nozzle, the contact with the substrate leads to important cooling. The strand undergoes an asymmetrical cooling from the bottom to the top. This kind of cooling has been already observed by Ravoori et al. [24] with an infrared video camera. The cooling seen by Ravoori et al. [24] is more important that in our case. Nevertheless, the velocity ratio U/V is not specified in [24].

The temperature field in the strand cross section decreases progressively in the x direction resulting from the balance between the advection and the thermal conduction through the strand. Figure 16 provides the temperature field in the symmetric plane (x, z) and in a cross section localised at x=3.23 mm for g/D equal to 1.625. A sharp temperature decrease is observed within a few millimetres. This trend is more pronounced when the gap decreases.

(a) (x, z) plane

(b) (y, z) plane at x=3.23 mm



Figure 15: Temperature field for g/D equal to 0.75 (a) in the symmetric plane (x, z) and (b) in a cross section localised at x=3.23 mm from the exit of the nozzle.

(a) (x, z) plane

(b) (y, z) plane at x=3.23 mm

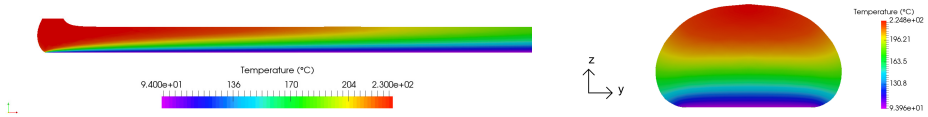


Figure 16: Temperature field for g/D equal to 1.625 (a) in the symmetric plane (x, z) and (b) in a cross section localised at x=3.23 mm from the exit of the nozzle.

After a certain distance from the nozzle exit, the temperature gradient is mainly present along the z axis. The maximum temperature in the strand is lower for the strand with the lowest height. The strand cooling seems mainly driven by conduction with the substrate.

To investigate the thermal behaviour along the x axis, numerical computations have been done for other working conditions changing the gap and the velocity ratio. The temperature profile is taken in the middle of the strand. Figure 17a presents the behaviour of θ as a function of x. After a short area localised under the nozzle where the temperature is quasi equal to one, a cooling is observed along the longitudinal axis. No clear trend raises as a function of the working conditions of the printer.

The cooling of the strand has been analysed by Bellehumeur et al. [20] accounting for the heat transfer between the polymer and the surrounding air and the substrate. This model depends on the perimeter $\mathcal{P}$ and the area of the cross section, A. Here the original model of Bellehumeur et al. [20] is improved by considering the thermal transfer between the polymer and the surrounding air and the polymer and the substrate separately. Using a 1-D description of the deposited strand, the average temperature over a cross section, $\bar{\theta}$, obeys to the simple ordinary differential equation

$$\frac{d^2\bar{\theta}}{dx^2} - \mathrm{Pe}\,\frac{d\bar{\theta}}{dx} - \frac{\mathcal{P}}{A}\left[\chi_{\mathrm{air}}\,\mathrm{Bi}_{\mathrm{air}} + (1-\chi_{\mathrm{air}})\,\mathrm{Bi}_{\mathrm{sub}}\right]\bar{\theta} = -\frac{\mathcal{P}}{A}(1-\chi_{\mathrm{air}})\,\mathrm{Bi}_{\mathrm{sub}}\,\theta_{\mathrm{sub}}, \tag{16}$$

with Pe the Péclet number already defined by (15), χ_{air} the ratio of the perimeter in contact only with surrounding air to the total perimeter and θ_{sub} is the reduced temperature of the substrate. The two dimensionless numbers, $\mathrm{Bi}_{\mathrm{air}}$, and $\mathrm{Bi}_{\mathrm{sub}}$ are the Biot

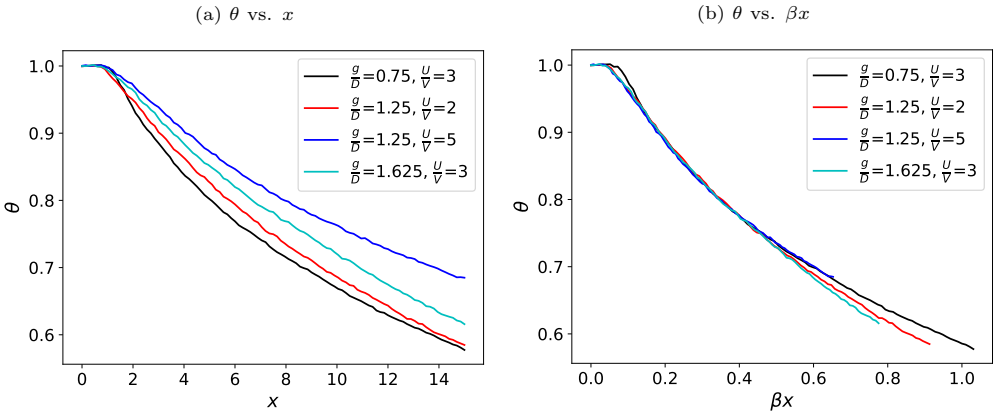


Figure 17: Temperature behaviour in the middle of the strand as a function of x in (a) and βx in (b).

numbers defined by

$$\mathrm{Bi}_{\mathrm{air}} = \frac{h_{\mathrm{air}} g}{k_p}, \tag{17}$$

$$\mathrm{Bi}_{\mathrm{sub}} = \frac{h_{\mathrm{sub}} g}{k_p}, \tag{18}$$

with h_{air} and the h_{sub} air/polymer and polymer/substrate heat transfer coefficients, respectively. Equation (16) is written under dimensionless form with the characteristic scales introduced in the numerical section.

The integration of (16) gives the following solution

$$\bar{\theta} = \left[1 - \frac{(1-\chi_{\mathrm{air}})\,\mathrm{Bi}_{\mathrm{sub}}\,\theta_{\mathrm{sub}}}{\chi_{\mathrm{air}}\,\mathrm{Bi}_{\mathrm{air}} + (1-\chi_{\mathrm{air}})\,\mathrm{Bi}_{\mathrm{sub}}}\right] e^{-\beta x} + \frac{(1-\chi_{\mathrm{air}})\,\mathrm{Bi}_{\mathrm{sub}}\,\theta_{\mathrm{sub}}}{\chi_{\mathrm{air}}\,\mathrm{Bi}_{\mathrm{air}} + (1-\chi_{\mathrm{air}})\,\mathrm{Bi}_{\mathrm{sub}}}, \tag{19}$$

for $x > 0$ and β given by

$$\beta = \frac{\mathrm{Pe}}{2}\left(\sqrt{1 + \frac{4\mathcal{P}}{A\,\mathrm{Pe}^2}\left[\chi_{\mathrm{air}}\,\mathrm{Bi}_{\mathrm{air}} + (1-\chi_{\mathrm{air}})\,\mathrm{Bi}_{\mathrm{sub}}\right]} - 1\right). \tag{20}$$

Equation (19) suggests that the temperature should be scaled as a function of βx. Figure 17b represents the behaviour of the temperature as a function of βx. A general curve clearly appears under this form. The various values of β have been determined using the data of the Pe, $\mathcal{P}$, A, χ_{air}, $\mathrm{Bi}_{\mathrm{air}}$ and $\mathrm{Bi}_{\mathrm{sub}}$ given in Table 4. To obtain the single curve, χ_{air} and the Biot numbers have been estimated. To determine χ_{air}, the strand shape is assumed oblong. From the correlations found in the previous section, it is easy to estimate χ_{air}. According to Agassant et al. [25, page 239], the heat transfer due to natural

Table 4: Values of Pe, $\mathcal{P}$, A, χ_{air}, Bi_{air} and Bi_{sub} for the four numerical cases used to determine β, eq. (20).

Case	Pe	$\mathcal{P}$	A	χ_{air}	Bi_{air}	Bi_{sub}
$\frac{g}{D}$=0.75, $\frac{U}{V}$=3	28.857	6.210	4.023	0.685	4.28×10^{-2}	4
$\frac{g}{D}$=1.25, $\frac{U}{V}$=2	48.095	2.641	0.961	0.817	7.142×10^{-2}	5.5
$\frac{g}{D}$=1.25, $\frac{U}{V}$=5	48.095	4.494	2.442	0.783	7.142×10^{-2}	5
$\frac{g}{D}$=1.625, $\frac{U}{V}$=3	62.523	2.490	0.852	0.871	9.286×10^{-2}	8

convection for an horizontal cylinder is around $16\,\text{Wm}^{-2}\text{K}^{-1}$. The contribution due to thermal radiation is around $13\,\text{Wm}^{-2}\text{K}^{-1}$ [25, page 246]. Therefore, the heat transfer coefficient between the surrounding air and the polymer is set equal to $30\,\text{Wm}^{-2}\text{K}^{-1}$ as already used by Thomas and Rodríguez [26] and by Bellehumeur et al. [20]. The Biot number of the heat transfer between the polymer and the substrate has been adapted to have a good agreement between the numerical solution and the predicted solution given by (19). The respective values of Bi_{sub} are gathered in Table 4. As expected the heat transfer between the polymer and substrate is more efficient than the heat transfer between the polymer and surrounding air. From these data, heat transfer coefficients between the polymer and the substrate are around $2 \times 10^3\,\text{Wm}^{-2}\text{K}^{-1}$.

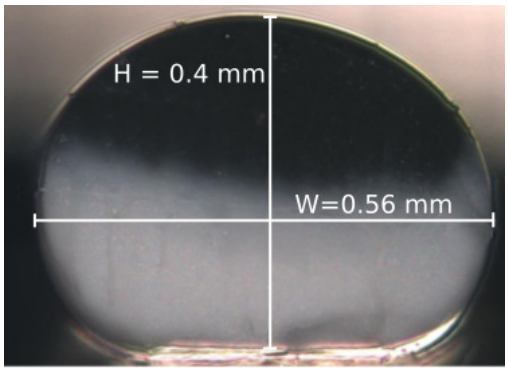
Even if the comparison to this simple model is done by taking a temperature in the middle of the strand, the agreement with the theory is acceptable. This simple model pinpoints that the perimeter and the area of the cross section are the relevant parameters to describe the thermal cooling of the deposited strand. With the approximate relations determining the width and height of a strand, it is possible to implement a simple model to study the thermal cooling as developed for instance by Costa et al. [27]. When the substrate is substituted by a previously deposited layer the heat transfer will significantly decrease. The macroscopic model used by Xu et al. [15] showed lower heat transfer coefficients than the values indicated here.

4. Comparison between numerical predictions of strand dimensions and experiments

The computed strand height and width are compared to experimental measurements. The printing velocity V is equal to $1\,\text{m}\,\text{min}^{-1}$. The nozzle diameter is equal to 0.4 mm. As previously, the substrate, the nozzle and the air temperatures are set to 94, 230 and 40 °C. The comparison is achieved for various U/V ratios and two ratios g/D equal to 1.25 and 1.625.

In Figure 18, the strand shape obtained numerically is compared with the experimental one printed at U/V equal to 2 and g/D equal to 1.625. The cross section of the

(a) Experiment



(b) Num. simul.

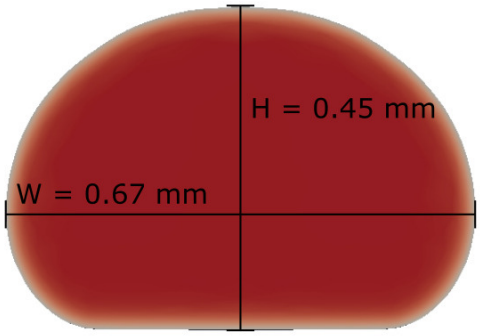
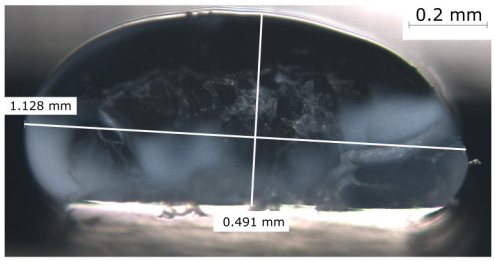


Figure 18: Experimental (a) and numerical (b) cross sections obtained for U/V equal to 2 and g/D equal to 1.625.

(a) Experiment



(b) Num. simul.

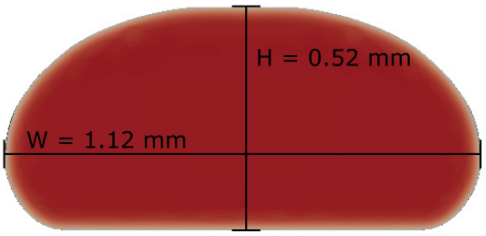


Figure 19: Experimental (a) and numerical (b) cross sections obtained for U/V equal to 4 and g/D equal to 1.625.

deposited filament presents an asymmetric cross section. While the part in contact with the substrate is very similar to an oblong shape, the opposite part is more similar to the elliptic shape. This asymmetry is numerically very well captured. The numerical result overestimates both the width and the height of the strand cross section.

An equivalent comparison is done in Figure 19 for U/V equal to 4 and the same g/D ratio. The strand is wider and higher for U/V equal to 4 than for U/V equal to 2. This expected result is in agreement with experiments analysed in § 2.3. The asymmetric cross section and the dimensions of the strand are very well reproduced numerically.

Figure 20a presents the behaviour of W/D as a function of $\sqrt{\alpha}$ with α defined by equation (5). Both experimental measurements and numerical computations have been collected. These data are obtained for g/D equal to 1.25 in blue colour and for 1.625 in red colour. The average deviation between the simulated strand width and the experimental measurements is around 5 % for both gaps. The black solid line corresponds to the approximate solution given by equation (6). It provides a very relevant approximation.

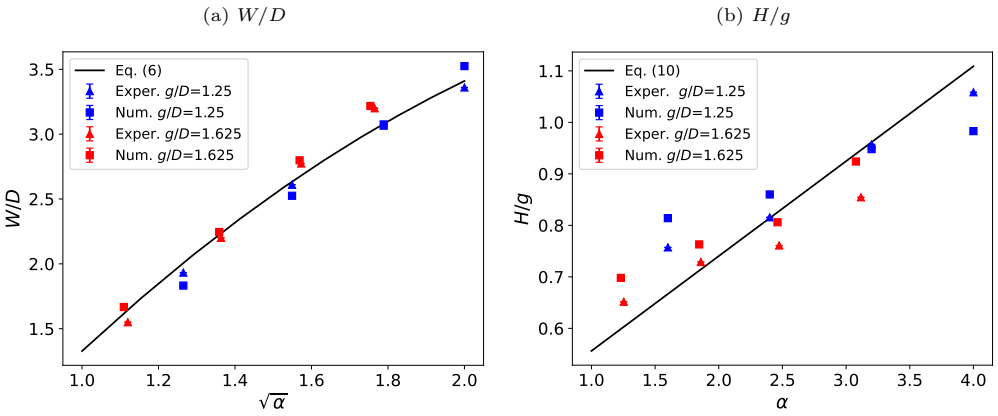


Figure 20: (a) W/D vs. $\sqrt{\alpha}$ and (b) H/g vs. α obtained numerically and experimentally for g/D equal to 1.25 and 1.625.

Figure 20b depicts H/g as a function of α for the same series of data. The deviation ranges from 1 to 8 % with an average deviation of 5.9 %. The black solid line is the fitted function given by equation (10). It is less relevant than the width prediction.

The numerical method set in this work reproduces the main physical features observed experimentally. However, the fluid mechanics has been simplified since the viscoelasticity behaviour has not been taken into account. The thermal conditions are also idealised.

5. Synthesis and perspectives

This paper provides extensive measurements of the strand dimensions obtained with the material extrusion process. The parameters of highest influence were investigated including (i) the extrusion velocity U, (ii) printing velocity V, (iii) gap between the substrate and the tip of the nozzle g, (iv) nozzle diameter D. In a previous paper [8], it is shown that the width of the deposited strand is a function of $\alpha = (D/g)(U/V)$ using a simplified analytical model. In this paper, the W/D and H/g ratios are gathered within single curves function of this parameter α.

A numerical model of the deposition process is developed assuming a temperature dependent purely viscous model. The computed widths and heights of the deposited strand agree well with the experimental measurements. The computations performed for two g/D ratios and a wide range of U/V ratios show a good agreement (less than 6% difference) with the corresponding experiments. This confirms the relevance of the parameter α to define the width and the height of the deposited strand as a function of the printing parameters.

Moreover, the numerical model provides interesting complementary results, as for

example the precise shape of the deposited strand. The applied pressure (or stress) on the substrate as well as the temperature field between the printing head and the substrate are leading parameters for the welding capacities with the previous deposited strands. The thermal cooling after the deposition pinpoints that a unified process can be established. This analysis underlines the importance to know the perimeter and the area of the strand.

This paper opens the route for three different perspectives in FFF additive manufacturing modelling: (i) Confront the numerical model to a wider range of experimental strand measurements, especially for low g/D ratios which showed a singular behaviour; (ii) Provide a global computation of the FFF process, including the melting process in the liquefier. As underlined in a previous paper [14], a marked radial temperature gradient at the end of the liquefier may be observed at high extrusion velocity. This will impact the succeeding printing process; (iii) Introduce viscoelastic constitutive equations which will essentially impact die swelling at the nozzle exit. This should induce confinement and pressure development between the printing head and the substrate, even for gap dimensions larger than the nozzle diameter.

CRediT author statement

D. Xu: Investigation, Methodology, Validation, Formal analysis, Software, Writing - Original Draft. **J.-F. Agassant**: Conceptualisation, Formal analysis, Writing - Review & Editing. **F. Pigeonneau**: Conceptualisation, Formal analysis, Software, Writing - Review & Editing, Supervision.

Declaration of Competing Interest

The authors declare that they have no known competing financial interests or personal relationships that could have appeared to influence the work reported in this article.

Acknowledgements

The authors are indebted to Sarah Marion who did experiments during her Master-thesis internship in our lab. We are grateful to Julien Férec (IRDL, university of Bretagne, France) and Nicolas Boyard (LTEN, university of Nantes, France) for their valuable advice and urge us to publish our work.

Appendix A. Nomenclature

	Upper-case roman	
A	Area of the cross section of a strand	m^2
$\mathrm{Bi}_{\mathrm{air}}$	Biot number for the heat transfer with air	–
$\mathrm{Bi}_{\mathrm{sub}}$	Biot number for the heat transfer with substrate	–
Ca	Capillary number	–
C_p	Specific heat capacity	$\mathrm{J\,kg^{-1}\,K^{-1}}$
C_{p_p}	Specific heat capacity of the polymer	$\mathrm{J\,kg^{-1}\,K^{-1}}$
D	Diameter of the nozzle	m
E	Thickness of the truncation in the filtered level-set function	m
E_a	Activation energy	$\mathrm{J\,mol^{-1}}$
$\mathcal{H}$	Heaviside function	–
H	Height of a unique strand	m
L	Length of front spreading of the polymer	m
P	Pressure	Pa
$\mathcal{P}$	Perimeter of a strand cross section	m
Pe	Péclet number	–
R	Ideal gas constant	$\mathrm{J\,mol^{-1}\,K^{-1}}$
Re	Reynolds number	–
R_{in}	Radius of the inlet cylinder of the nozzle	m
R_n	External radius of the nozzle	m
T	Temperature	K, °C
T_{air}	Surrounding air temperature	K, °C
T_{ext}	Temperature of the extruder	K, °C
T_g	Glass transition temperature	K, °C
T_{ref}	Reference temperature of the shift factor	K
T_{sub}	Temperature of the substrate	K, °C
U	Extrusion velocity	$\mathrm{m\,s^{-1}}$
U_{in}	Inlet average velocity at the inlet of the extruder	$\mathrm{m\,s^{-1}}$
V	Printing velocity	$\mathrm{m\,s^{-1}}$
W	Width of a unique strand	m
Wi	Weissenberg number	–
	Lower-case roman	
a	Yasuda coefficient	–
a_T	Shift factor	–
d_Γ	Euclidean distance from the interface Γ	m
g	Distance between the substrate and the tip of the nozzle	m
h_{air}	Air/polymer heat transfer coefficient	$\mathrm{Wm^{-2}K^{-1}}$

h_{sub}	Polymer/substrate heat transfer coefficient	$\mathrm{W m^{-2} K^{-1}}$
k	Thermal conductivity	$\mathrm{W\,m^{-1}\,K^{-1}}$
k_p	Thermal conductivity of the polymer	$\mathrm{W\,m^{-1}\,K^{-1}}$
m	Shear thinning index	–
$\boldsymbol{n}$	Outer unit normal	–
$\boldsymbol{n}_\Gamma$	Unit normal at the interface	–
r	Radial coordinate in the nozzle	m
t	Time	s
$\boldsymbol{u}$	Velocity	$\mathrm{m\,s^{-1}}$
$\boldsymbol{x}$	Cartesian coordinate	m
x	Longitudinal Cartesian coordinate	m
y	Transversal Cartesian coordinate	m
z	Vertical Cartesian coordinate	m
	Upper-case greek	
Γ	Interface between the two phases	–
Ω	Computational space domain	–
$\partial\Omega_{\text{noz}}$	Nozzle surface of computational space domain	–
$\partial\Omega_{\text{sub}}$	Substrate surface of computational space domain	–
Ω_g	Computational space domain of gas	–
$\partial\Omega_g^{\text{in}}$	Inlet surface of gas	–
$\partial\Omega_g^{\text{out}}$	Outlet surface of gas	–
Ω_p	Computational space domain of polymer	–
	Lower-case greek	
α	Dimensionless group equal to $DU/(gV)$	–
β	Dimensionless coefficient	–
γ	Surface tension	$\mathrm{N\,m^{-1}}$
$\dot{\gamma}$	Shear rate	$\mathrm{s^{-1}}$
δ	Dirac function	$\mathrm{m^{-1}}$
ϵ	Numerical coefficient	m
$\dot{\boldsymbol{\varepsilon}}$	Rate-of-strain tensor	$\mathrm{s^{-1}}$
η	Dynamical viscosity	Pa s
η_0	Dynamical viscosity at zero shear rate	Pa s
θ	Dimensionless temperature	–
$\bar{\theta}$	Cross sectional average temperature	–
θ_{sub}	Dimensionless temperature of the substrate	–
κ_Γ	Mean curvature	$\mathrm{m^{-1}}$
λ	Relaxation time	s

μ	Numerical parameter of the Hamilton-Jacobi equation	–
ρ	Density	kg/m^3
ρ_p	Density of the polymer	kg/m^3
φ	Level-set function	m
$\tilde{\varphi}$	Filtered level-set function	m
χ_{air}	fraction of the perimeter in contact with surrounding air	–

Appendix B. Numerical computation of a filament deposition

Appendix B.1. Governing equations

The numerical computation focuses on the extrusion and deposition of a single strand. Only the inside tip of the nozzle is considered. As displayed in Figure 6, it is composed of the end of the liquefier, the convergent region and the final capillary region of the nozzle. The problem is symmetric along the perpendicular plane of the substrate, cutting the printer in two parts. Therefore, only one half of the domain is considered. The nozzle solid domain and the substrate are not included in the numerical domain and only the polymer and air domains are considered in the computation.

An open space domain Ω is composed of two open subdomains, $\Omega_p(t)$ where the polymer is present and $\Omega_g(t)$ corresponding to the surrounding air. Figure 6 depicts a cross section in the symmetric plane $x-z$ of the domain in which $\Omega_p(t)$ and $\Omega_g(t)$ are represented in the initial conditions. The reference frame is attached to the extruder with x axis directed downstream, z along the axis of the extruder and y perpendicular to the symmetry plane. The wall of the substrate, $\partial\Omega_{\text{sub}}$, slides in the opposite direction of the "real" motion of the extruder at constant velocity. This change of Galilean reference frame needs to consider that the air phase enters in the domain with a velocity equal to the printing velocity through the boundary $\partial\Omega_g^{\text{in}}$. The domain is extended over a distance $5g$ upstream and $15g$ downstream of the extruder. Transversely, the domain width is set equal to $5g$.

The interface between the two phases is simply given by $\Gamma(t) = \partial\bar{\Omega}_p(t) \cap \partial\bar{\Omega}_g(t)$ [28]. To follow the two phases and the interface $\Gamma(t)$, the two-phase fluid dynamics is described as a single-fluid representation [29]. Each phase is flagged by a characteristic function. To determine these functions, the position of the interface between the two phases is used by taking the level-set (distance) function defined as follows [17]

$$\varphi(\boldsymbol{x},t) = \begin{cases} d_\Gamma(\boldsymbol{x}) & \forall\ \boldsymbol{x} \in \Omega_p(t), \\ 0 & \forall\ \boldsymbol{x} \in \Gamma(t), \\ -d_\Gamma(\boldsymbol{x}) & \forall\ \boldsymbol{x} \in \Omega_g(t), \end{cases} \tag{B.1}$$

in which $d_\Gamma(\boldsymbol{x})$ is the Euclidean distance from the interface $\Gamma(t)$. Mathematically, the characteristic function for the polymer is $\mathcal{H}(\varphi(\boldsymbol{x},t))$ corresponding to the generalised Heaviside function. The complementary function $1-\mathcal{H}(\varphi(\boldsymbol{x},t))$ corresponds to the characteristic function of the air subdomain. In the single-fluid representation, a generic function ψ is then written as follows

$$\psi = \mathcal{H}(\varphi(\boldsymbol{x},t))\psi_p + [1-\mathcal{H}(\varphi(\boldsymbol{x},t))]\psi_g, \tag{B.2}$$

with ψ_p and ψ_g the properties in subdomains Ω_p and Ω_g respectively.

The governing equations are written under dimensionless form. Spatial coordinates are normalised by the gap g between the substrate and the nozzle. The printing velocity V is used to normalise the velocity field and g/V for time. The density, thermal conductivity, specific heat capacity and dynamic viscosity are normalised by ρ_p, k_p, C_{p_p} and η_0, respectively. Since temperature ranges from the surrounding air temperature T_{air} and the extrusion temperature T_{ext}, it is normalised as follows

$$\theta = \frac{T-T_{\text{air}}}{T_{\text{ext}}-T_{\text{air}}}. \tag{B.3}$$

Using the general method presented in [29], the governing equations are the following:

$$\boldsymbol{\nabla}\cdot\boldsymbol{u} = 0, \tag{B.4}$$

$$\text{Re}\,\rho\frac{D\boldsymbol{u}}{Dt} = -\boldsymbol{\nabla}P + \boldsymbol{\nabla}\cdot[2\eta(\theta,\dot{\gamma})\dot{\boldsymbol{\varepsilon}}] + \frac{1}{\text{Ca}}\kappa_\Gamma\delta(\varphi)\|\boldsymbol{\nabla}\varphi\|\boldsymbol{n}_\Gamma, \tag{B.5}$$

$$\rho C_p\frac{D\theta}{Dt} = \frac{1}{\text{Pe}}\boldsymbol{\nabla}\cdot(k\boldsymbol{\nabla}\theta), \tag{B.6}$$

with

$$\dot{\boldsymbol{\varepsilon}} = \frac{1}{2}\left(\boldsymbol{\nabla}\boldsymbol{u}+\boldsymbol{\nabla}^t\boldsymbol{u}\right), \tag{B.7}$$

$$\dot{\gamma} = \sqrt{2\dot{\boldsymbol{\varepsilon}}:\dot{\boldsymbol{\varepsilon}}}. \tag{B.8}$$

Equation (B.4) means that the volume is conserved. Both polymer and air are then assumed incompressible. Moreover, no mass transfer is considered between the two fluids. In the momentum equation, (B.5), gravity forces are neglected since the characteristic scales are small. The last source term in the right-hand side of (B.5) corresponds to the surface tension force for which $\delta(\varphi)$ is the Dirac function of φ. The unit normal at the

interface $\Gamma(t)$ and the mean curvature are defined by

$$\boldsymbol{n}_\Gamma = \frac{\boldsymbol{\nabla}\varphi}{\|\boldsymbol{\nabla}\varphi\|}, \tag{B.9}$$

$$\kappa_\Gamma = -\boldsymbol{\nabla}\cdot\boldsymbol{n}_\Gamma. \tag{B.10}$$

In the energy equation the viscous dissipation has been neglected.

The Reynolds number, Re, the capillary number, Ca, and the Péclet number, Pe have been already defined in § 3. The dynamic viscosity of the molten polymer fitted by Carreau-Yasuda law takes the following dimensionless form

$$\eta_p(\dot{\gamma},\theta) = \frac{a_T}{[1+(\mathrm{Wi}\,a_T\dot{\gamma})^a]^{(1-m)/a}}, \tag{B.11}$$

with Wi the Weissenberg number defined by equation (15).

In absence of mass transfer, the interface $\Gamma(t)$ is a material surface moving at the fluid velocity meaning that the transport of the interface is simply given by the equation

$$\frac{\partial\varphi}{\partial t} + \boldsymbol{u}\cdot\boldsymbol{\nabla}\varphi = 0. \tag{B.12}$$

Nevertheless, as it is well known, the transport of φ using the previous equation leads to the loss of the Eikonal property of φ, i.e. $\|\boldsymbol{\nabla}\varphi\| \neq 1$ [18]. A reinitialisation of the level-set function is then needed after the transport step. Sethian and Smereka [18] reviewed the various techniques used to do the reinitialisation. Here, the method proposed by Ville et al. [30] has been selected. The transport and reinitialisation steps are achieved in a unique transport equation with an additional source term in the Hamilton-Jacobi equation given by [30]

$$\frac{\partial\varphi}{\partial t} + \boldsymbol{u}\cdot\boldsymbol{\nabla}\varphi = \mathrm{sign}(\varphi)\mu\left(1-||\boldsymbol{\nabla}\varphi||\right), \tag{B.13}$$

with $\mathrm{sign}(\varphi)$ the sign function of φ and μ a numerical parameter chosen as a function of the mesh size and the time step. Furthermore, a filtered level-set function is defined as follows

$$\tilde{\varphi} = E\tanh\left(\frac{\varphi}{E}\right), \tag{B.14}$$

in which E is the thickness of the truncation. With this definition, it is easy to see that

$$\|\boldsymbol{\nabla}\tilde{\varphi}\| = 1 - \left(\frac{\tilde{\varphi}}{E}\right)^2, \tag{B.15}$$

meaning that close to the interface the Eikonal property is fulfilled.

As proposed by Bonito et al. [31], the combination of (B.13) and (B.15) gives the self-reinitialisation level set equation

$$\frac{\partial \tilde{\varphi}}{\partial t} + \boldsymbol{u} \cdot \boldsymbol{\nabla} \tilde{\varphi} = \mu \text{sign}(\tilde{\varphi}) \left[1 - \left(\frac{\tilde{\varphi}}{E} \right)^2 - \|\boldsymbol{\nabla} \tilde{\varphi}\| \right], \tag{B.16}$$

which is used in the numerical computation to transport $\tilde{\varphi}$.

Appendix B.2. Boundary conditions

The nozzle geometry corresponds to the E3D-V6 nozzle with a final capillary diameter of D equal to 0.4 mm (see ref. [16] for more details about the geometry E3D-V6 extruder). It forms the boundary $\partial\Omega_{\text{noz}}$ of the computation domain. The bottom surface of the domain $\partial\Omega_{\text{sub}}$ is the substrate. The other boundaries ($\partial\bar{\Omega}_g$, $\partial\Omega_g^{\text{in}}$, $\partial\Omega^{\text{out}}$) are in contact with air.

In the initial state, the interior of the nozzle is full of polymer and immersed in the computation domain. This immersed domain Ω_p (in orange in Figure 6) is then taken as the initial polymer domain. The rest of the computation domain Ω_g is considered as surrounding air.

As already mentioned above, the nozzle is immobile and a constant velocity is applied on the substrate in the x direction. A no-slip condition is considered on the substrate and nozzle boundaries. At the inlet polymer boundary $\partial\Omega_p$, a Poiseuille velocity profile is imposed such that:

$$u_z(r) = -2U_{\text{in}} \left[1 - \left(\frac{r}{R_{\text{in}}} \right)^2 \right], \tag{B.17}$$

with U_{in} the inlet average velocity given by

$$U_{\text{in}} = U \left(\frac{D}{2R_{\text{in}}} \right)^2, \tag{B.18}$$

with R_{in} the radius of the inlet cylinder and r the radius coordinate equal to $\sqrt{x^2 + y^2}$.

As the nozzle moves in the x^- direction, a convective flow of air equal to the printing velocity is applied on the boundary $\partial\Omega_g^{\text{in}}$. No condition is applied on the $\partial\Omega^{\text{out}}$. On the other air boundaries, the impermeable condition is applied meaning that $\boldsymbol{u} \cdot \boldsymbol{n} = 0$ with $\boldsymbol{n}$ the outer unit normal.

In the initial state, the air domain Ω_g and the polymer domain Ω_p have an imposed temperature $\theta = 0$ and $\theta = 1$, respectively. The inlet polymer has an imposed temperature of $\theta = 1$. In the nozzle boundary $\partial\Omega_{\text{noz}}$, Dirichlet boundary condition is used such as $\theta = 1$. In upstream air boundary $\partial\Omega_g^{\text{in}}$ has an imposed temperature $\theta = 0$. The

substrate boundary $\partial\Omega_{sub}$ has an imposed temperature equal to

$$\theta_{\text{sub}} = \frac{T_{\text{sub}} - T_{\text{air}}}{T_{\text{ext}} - T_{\text{air}}}. \tag{B.19}$$

The temperature jumps at the intersection $\partial\Omega_g^{\text{in}} \cap \partial\Omega_{\text{sub}}$ leads to computation instabilities. To ensure the continuity of the boundary condition at this edge, the temperature is set equal to

$$\theta = \theta_{\text{sub}} \left[1 - \exp\left(- \frac{|x - x_{\partial\Omega_g^{\text{in}} \cap \partial\Omega_{\text{sub}}}|}{\epsilon} \right) \right], \tag{B.20}$$

in which ϵ is a numerical coefficient controlling how fast the temperature changes from 0 to θ_{sub}.

The filtered level set must be imposed in boundaries where the fluid goes inside the domain. The boundary conditions are then

$$\tilde{\varphi} = -E, \ \forall \boldsymbol{x} \in \partial\Omega_g^{\text{in}}, \tag{B.21}$$

$$\tilde{\varphi} = E, \ \forall \boldsymbol{x} \in \partial\Omega_p. \tag{B.22}$$

For the rest of boundaries, the homogeneous Neumann condition is applied. At the substrate boundary, $\partial\Omega_{\text{sub}}$, where a triple line is present (substrate/air/polymer), the contact angle is then equal to $\pi/2$.

All boundary conditions for the three equations are summarised in Table B.6.

Table B.6: Boundary conditions of fluid mechanics, heat transfer and level set equations in the boundaries of the computational domain depicted in Figure 6.

Boundary	Fluid mech.	Heat transfer	Level set
$\partial\Omega_{\text{noz}}$	$\boldsymbol{u} = 0$	$\theta = 1$	$\frac{\partial\tilde{\varphi}}{\partial n} = 0$
$\partial\bar{\Omega}_g / \partial\Omega_g^{\text{in}} \cup \partial\Omega^{\text{out}}$	$\boldsymbol{u} \cdot \boldsymbol{n} = 0$	$\frac{\partial\theta}{\partial n} = 0$	$\frac{\partial\tilde{\varphi}}{\partial n} = 0$
$\partial\Omega_g^{\text{in}}$	$\boldsymbol{u} = \boldsymbol{e}_x$	$\theta = 0$	$\tilde{\varphi} = -E$
$\partial\Omega_{\text{sub}}$	$\boldsymbol{u} = \boldsymbol{e}_x$	Eq. (B.20)	$\frac{\partial\tilde{\varphi}}{\partial n} = 0$
$\partial\Omega_p$	$\boldsymbol{u} = -2U_{\text{in}} \left[1 - \left(\frac{r}{R_{\text{in}}} \right)^2 \right] \boldsymbol{e}_z$	$\theta = 1$	$\tilde{\varphi} = E$

Appendix B.3. Numerical method

Numerical computations are achieved with our own `C++ CimLib` library. To solve the system of equations (B.4-B.6) and (B.16), a time-marching method is used. To determine the temporal derivatives of $\boldsymbol{u}$, θ and $\tilde{\varphi}$, a finite-difference method at the first order

is employed. To ensure the stability of the scheme, an implicit Euler scheme is implemented. The spatial discretisation is achieved by a finite-element method. The domain is discretised with linear tetrahedron elements. For Navier-Stokes equations, the discrete inf−sup condition is satisfied by using the element $\mathbb{P}_1-$bubble$/\mathbb{P}_1$ [32]. The temperature and level-set transport equations are stabilised by a Streamline Upwind/Petrov-Galerkin method [33]. The polymer/air interface must be defined with the most accuracy. An anisotropic adaptive meshing is achieved. The filtered level set field is taken as criterion. The sharp gradients are captured using an *a posteriori* error estimation based on the length distribution tensor approach and the associated edge based error estimator (see [34], for more details). The mesh adaptation is performed after each time step.

Initially, the polymer domain is immersed in the computation domain by incorporating a mesh fitting with the geometry of the nozzle. A level set function is then created based on the immersed domain. The temperature is then imposed in the polymer and air domains based on the level set function. The viscosity of the polymer at rest is then computed using the temperature dependence.

At each time step, the polymer viscosity is computed based on temperature and rate of strain fields of the previous time step. The generalized Navier-Stokes equations are then solved with the material properties corresponding to their respective domains. The attribution is based on the level set function computed at the previous increment using a regularised Heaviside function. The heat transfer equation is then solved. Finally, the level set function is transported based on the computed velocity field. Finally, the mesh adaptation is done. The computation stops when the geometry of the deposited strand is stabilised.

References

[1] A. Bellini, S. Güçeri, and M. Bertoldi. Liquefier dynamics in fused deposition. *J. Manuf. Sci. Eng.*, 126(2):237–246, 2004.

[2] A. Bellini. *Fused Deposition of Ceramics: A Comprehensive Experimental, Analytical and Computational Study of Material Behavior, Fabrication Process and Equipment Design.* PhD thesis, Faculty of Drexel University, Philadelphie, September 2002.

[3] M. Hebda, C. McIlroy, B. Whiteside, F. Caton-Rose, and P. Coates. A method for predicting geometric characteristics of polymer deposition during Fused-Filament-Fabrication. *Addit. Manuf.*, 27:99–108, 2019.

[4] R. Comminal, M. P. Serdeczny, D. B. Pedersen, and J. Spangenberg. Numerical modeling of the strand deposition flow in extrusion-based additive manufacturing. *Addit. Manuf.*, 20:68–76, 2018.

[5] M. P. Serdeczny, R. Comminal, D. B. Pedersen, and J. Spangenberg. Experimental validation of a numerical model for the strand shape in material extrusion additive manufacturing. *Addit. Manuf.*, 24:145–153, 2018.

[6] A. Gosset, D. Barreiro-Villaverde, J. C. Becerra Permuy, M. Lema, A. Ares-Pernas, and M. J. Abad

López. Experimental and Numerical Investigation of the Extrusion and Deposition Process of a Poly(lactic Acid) Strand with Fused Deposition Modeling. *Polymers*, 12(12):2885, 2020.

[7] B. Behdani, M. Senter, L. Mason, M. Leu, and J. Park. Numerical study on the temperature-dependent viscosity effect on the strand shape in extrusion-based additive manufacturing. *J. Manuf. Mater. Process.*, 4(2):46, 2020.

[8] J.-F. Agassant, F. Pigeonneau, L. Sardo, and M. Vincent. Flow analysis of the polymer spreading during extrusion additive manufacturing. *Addit. Manuf.*, 29:100794, 2019.

[9] H. Xia, J. Lu, S. Dabiri, and G. Tryggvason. Fully resolved numerical simulations of fused deposition modeling. Part I: fluid flow. *Rapid Prototyp. J.*, 2018.

[10] H. Xia, J. Lu, and G. Tryggvason. Fully resolved numerical simulations of fused deposition modeling. Part II: Solidification, residual stresses and modeling of the nozzle. *Rapid Prototyp. J.*, 24(6):973–987, 2018.

[11] H. Xia, J. Lu, and G. Tryggvason. A numerical study of the effect of viscoelastic stresses in fused filament fabrication. *Comput. Methods Appl. Mech. Eng.*, 346:242–259, 2019.

[12] H. Xia, J. Lu, and G. Tryggvason. Simulations of fused filament fabrication using a front tracking method. *Int. J. Heat Mass Transfer*, 138:1310–1319, 2019.

[13] M. E. Mackay, Z. R. Swain, C. R. Banbury, D. D. Phan, and D. A. Edwards. The performance of the hot end in a plasticating 3D printer. *J. Rheol.*, 61(2):229–236, 2017.

[14] F. Pigeonneau, D. Xu, M. Vincent, and J.-F. Agassant. Heating and flow computations of an amorphous polymer in the liquefier of a material extrusion 3D printer. *Addit. Manuf.*, 32:101001, 2020.

[15] D. Xu, Y. Zhang, and F. Pigeonneau. Thermal analysis of the fused filament fabrication printing process: Experimental and numerical investigations. *Int. J. Mater. Form.*, 14(4):763–776, 2020.

[16] E3D-online. E3d help centre. https://e3d-online.zendesk.com/hc/en-us, 2021.

[17] J. A. Sethian. *Level set methods and fast marching methods. Evolving interfaces in computational geometry, fluid mechanics, computer vision, and materials science.* Cambridge University Press, Cambridge, 1999.

[18] J. A. Sethian and P. Smereka. Level set methods for fluid interfaces. *Annu. Rev. Fluid Mech.*, 35:341–371, 2003.

[19] J. U. Brackbill, D. B. Kothe, and C. Zemach. A continuum method for modeling surface tension. *J. Comput. Phys.*, 100(2):335–354, 1992.

[20] C. Bellehumeur, L. Li, Q. Sun, and P. Gu. Modeling of bond formation between polymer filaments in the fused deposition modeling process. *J. Manuf. Processes*, 6(2):170–178, 2004.

[21] J. Gavis and M. Modan. Expansion and contraction of jets of newtonian liquids in air: Effect of tube length. *Phys. Fluids*, 10(3):487–497, 1967.

[22] C. McIlroy and P. D. Olmsted. Deformation of an amorphous polymer during the fused-filament-fabrication method for additive manufacturing. *J. Rheol.*, 61(2):379–397, 2017.

[23] F. Yang and R. Pitchumani. Healing of Thermoplastic Polymers at an Interface under Nonisothermal Conditions. *Macromolecules*, 35(8):3213–3224, 2002.

[24] D. Ravoori, C. Lowery, H. Prajapati, and A. Jain. Experimental and theoretical investigation of heat transfer in platform bed during polymer extrusion based additive manufacturing. *Polym. Test.*, 73:439–446, 2019.

[25] J.-F. Agassant, P. Avenas, P. J. Carreau, B. Vergnes, and M. Vincent. *Polymer processing: principles and modeling.* Carl Hanser Verlag GmbH Co, 2017.

[26] J. P. Thomas and J. F. Rodriguez. Modeling the Fracture Strength between Fused-Deposition Extruded Roads 16. In *International Solid Freeform Fabrication Symposium*, 2000.

[27] S. F. Costa, F. M. Duarte, and J. A. Covas. Estimation of filament temperature and adhesion

development in fused deposition techniques. *J. Mater. Process. Technol.*, 245:167–179, 2017.

[28] S. Groß and A. Reusken. *Numerical methods for two-phase incompressible flows*, volume 40 of *Springer series in computational mathematics*. Springer-Verlag, Berlin, 2011.

[29] I. Kataoka. Local instant formulation of two-phase flow. *Int. J. Multiphase flow*, 12(5):745–758, 1986.

[30] L. Ville, L. Silva, and T. Coupez. Convected level set method for the numerical simulation of fluid buckling. *Int. J. Numer. Methods Fluids*, 66(3):324–344, 2011.

[31] A. Bonito, J.-L. Guermond, and S. Lee. Numerical simulations of bouncing jets. *Int. J. Numer. Meth. Fluids*, 80(1):53–75, 2016.

[32] A. Ern and J.-L. Guermond. *Theory and practice of finite elements*, volume 159. Springer Science & Business Media, 2004.

[33] A. N. Brooks and T. J. R. Hughes. Streamline upwind/Petrov-Galerkin formulations for convection dominated flows with particular emphasis on the incompressible Navier-Stokes equations. *Comput. Methods Appl. Mech. Engrg.*, 32(1):199–259, 1982.

[34] G. Jannoun, E. Hachem, J. Veysset, and T. Coupez. Anisotropic meshing with time-stepping control for unsteady convection-dominated problems. *Appl. Math. Modell.*, 39(7):1899–1916, 2015.